The Astronomical Journal, 163:96 (13pp), 2022 February https://doi.org/10.3847/1538-3881/ac402e

Mining the Ultrahot Skies of HAT-P-70b: Detection of a Profusion of Neutral and Ionized Species

Aaron Bello-Arufe[1], Samuel H. C. Cabot[2], João M. Mendonça[1], Lars A. Buchhave[1], and Alexander D. Rathcke[1]
[1] National Space Institute, Technical University of Denmark, Elektrovej, DK-2800 Kgs. Lyngby, Denmark; aarb@space.dtu.dk
[2] Yale University, 52 Hillhouse Avenue, New Haven, CT 06511, USA
Received 2021 September 3; revised 2021 November 27; accepted 2021 December 3; published 2022 January 27

Abstract

With an equilibrium temperature above 2500 K, the recently discovered HAT-P-70b belongs to a new class of exoplanets known as ultrahot Jupiters: extremely irradiated gas giants with day-side temperatures that resemble those found in stars. These ultrahot Jupiters are among the most amenable targets for follow-up atmospheric characterization through transmission spectroscopy. Here, we present the first analysis of the transmission spectrum of HAT-P-70b using high-resolution data from the HARPS-N spectrograph of a single-transit event. We use a cross-correlation analysis and transmission spectroscopy to look for atomic and molecular species in the planetary atmosphere. We detect absorption by Ca II, Cr I, Cr II, Fe I, Fe II, H I, Mg I, Na I, and V I, and we find tentative evidence of Ca I and Ti II. Overall, these signals appear blueshifted by a few km s^{-1}, suggestive of winds flowing at high velocity from the day side to the night side. We individually resolve the Ca II H and K lines, the Na I doublet, and the Hα, Hβ, and Hγ Balmer lines. The cores of the Ca II and H I lines form well above the continuum, indicating the existence of an extended envelope. We refine the obliquity of this highly misaligned planet to $107.9^{+2.0}_{-1.7}$ degrees by examining the Doppler shadow that the planet casts on its A-type host star. These results place HAT-P-70b as one of the exoplanets with the highest number of species detected in its atmosphere.

Unified Astronomy Thesaurus concepts: Exoplanet astronomy (486); Hot Jupiters (753); Exoplanets (498); Exoplanet atmospheric composition (2021); Exoplanet atmospheres (487); High resolution spectroscopy (2096); Transmission spectroscopy (2133); Extrasolar gaseous giant planets (509); Extrasolar gaseous planets (2172)

1. Introduction

Ultrahot Jupiters constitute the hottest class of exoplanets. The day sides of these extremely irradiated gas giants are characterized by temperatures well above 2000 K, reminiscent of those found in stars and hot enough to dissociate most molecular species (Arcangeli et al. 2018; Bell & Cowan 2018; Lothringer et al. 2018; Parmentier et al. 2018). Their high temperatures provide them with inflated atmospheres and a day-side and evening terminator that are mostly cloud-free and near chemical equilibrium (Heng 2016; Kitzmann et al. 2018; Gao et al. 2020; Helling et al. 2021). These exotic worlds are therefore ideal targets for atmospheric characterization through transmission spectroscopy.

Many of the current efforts to characterize ultrahot Jupiters involve ground-based observations with high-resolution spectrographs. These observations are revealing a large diversity of neutral and ionized atomic metals in ultrahot Jupiters (e.g., Hoeijmakers et al. 2019; Ben-Yami et al. 2020). The study of these refractory elements in transmission spectroscopy can inform us about the chemistry at the terminator region, the speed of the winds flowing between the day side and the night side, and potentially the formation and migration history of the planet (e.g., Ehrenreich et al. 2020; Nugroho et al. 2020b; Lothringer et al. 2021; Borsa et al. 2021; Kesseli & Snellen 2021).

HAT-P-70b is a recently discovered ultrahot Jupiter (Zhou et al. 2019). It has a mass of $M_p < 6.78\,M_J$, and it transits an A-type star with $T_{\rm eff} = 8450^{+540}_{-690}$ K every 2.74 days. At a distance of only 0.047 au from its host star, HAT-P-70b is subject to extreme stellar irradiation that elevates the equilibrium temperature of the exoplanet to $T_{\rm eq} = 2562^{+43}_{-52}$ K. Its large radius ($R_p = 1.87\,R_J$) and the brightness of its host star ($V = 9.47$) make HAT-P-70b a very favorable target for follow-up high-resolution transmission spectroscopy.

In this work we present the first analysis of the transmission spectrum of HAT-P-70b. We analyze high-resolution observations from a single-transit event observed with HARPS-N to search for absorption by atomic and molecular species via transmission spectroscopy and the cross-correlation technique (Snellen et al. 2010). This paper is structured in the following way: Section 2 describes the observations, data reduction, and telluric correction; Section 3 introduces our transmission spectroscopy and cross-correlation analyses, and how the Doppler shadow that results from the cross-correlation analysis is useful to refine the obliquity of HAT-P-70 b; Section 4 reports and discusses the results; and Section 5 presents the conclusions.

2. Observations and Data Reduction

HARPS-N is a high-resolution ($R \sim 115{,}000$), fiber-fed, cross dispersed echelle spectrograph covering the wavelength range between 3830 and 6930 Å(Cosentino et al. 2012). It is mounted on the 3.58 m Telescopio Nazionale Galileo (TNG) at the Observatorio del Roque de los Muchachos on the island of La Palma, Spain. Using HARPS-N, we observed a transit of HAT-P-70b on the night of 2020 December 18 between 21:28 and 02:10 UTC (program: A42TAC27, PI: A. Bello-Arufe). Although we were scheduled to observe until 03:00 UTC, technical issues related to the tracking of the telescope caused

the observations to stop earlier. Nevertheless, we still captured the full transit event, with sufficient out-of-transit baseline before and after the transit. We set the exposure time to 400 s, obtaining 40 exposures, 30 of which occurred during transit. Fiber A was placed on the target and fiber B on the sky. The night was clear with an average seeing of 0.″9–1.″0. The air masses of the different exposures were in the range 1.36–1.06–1.20.

The data were reduced using the HARPS-N Data Reduction Software (DRS), version 3.7. The main steps include bias and dark subtraction, bad-pixel and cosmic correction, flat-fielding, and wavelength calibration. Although the DRS also provides one-dimensional extracted spectra where the different orders are merged and rebinned, we only used these 1d spectra to produce the telluric model. In the rest of our analysis we used the two-dimensional (i.e., order by order) extracted spectra to avoid artifacts of order stitching. The signal-to-noise ratio (S/N) per pixel as measured by the DRS at the center of order 64 (the order with Hα) ranges from 28.5 to 51.2.

2.1. Telluric Correction

Gases in the atmosphere of the Earth produce absorption lines in spectra taken from ground-based observatories. In particular, the wavelength range covered by HARPS-N is affected by absorption predominantly due to oxygen and water. We used the software package `molecfit` version 1.5.9 (Kausch et al. 2015; Smette et al. 2015) to correct for these telluric absorption lines. `Molecfit` combines an atmospheric profile from the Global Data Assimilation System (GDAS) website and the line-by-line radiative-transfer code LBLRTM (Clough et al. 2005) to fit user-selected regions of the observed spectra and produce a synthetic transmission spectrum of the atmosphere of the Earth. `Molecfit` is frequently applied to HARPS-N data (e.g., Hoeijmakers et al. 2018; Casasayas-Barris et al. 2019; Wyttenbach et al. 2020; Stangret et al. 2021), and it is a more robust way to correct for telluric absorption than other empirical methods, e.g., using air mass (Langeveld et al. 2021).

We ran `molecfit` on the one-dimensional extracted spectra after Doppler-shifting them from the rest frame of the solar system barycenter to that of the observer. The regions that were included in the telluric fit were selected such that they covered a flat continuum with water and oxygen telluric features and without significant stellar absorption features. We fit a third-degree polynomial to the continuum of each spectral region. Given the high stability of HARPS-N, we did not re-calibrate the wavelength solutions of the different spectra. We found that values of 10^{-5} for both the relative χ^2 and parameter convergence criteria improved the quality of the fit. The telluric models produced by `molecfit` for each one-dimensional spectrum are then used to correct the two-dimensional spectra via linear interpolation. Figure 1 shows one of the one-dimensional spectra before and after telluric correction, including the spectral regions that were part of the fit.

3. Methods

In this section, we describe the methods we used to search for atomic and molecular species in the atmosphere of HAT-P-70b and how we derived the obliquity of the planet using its Doppler shadow.

3.1. The Cross-correlation Analysis

Since the discovery of carbon monoxide in the atmosphere of the hot Jupiter HD 209458b by Snellen et al. (2010), the cross-correlation technique has been commonly used to detect atomic and molecular species in the atmospheres of exoplanets from high-resolution spectra (see Birkby 2018, for an in-depth review of this method). Here, we followed a strategy similar to Hoeijmakers et al. (2020a) to search for metals in the atmosphere of HAT-P-70b.

We first Doppler-shifted the two-dimensional spectra by the barycentric velocity of the Earth, consequently shifting the spectra from the rest frame of the observatory to that of the solar system barycenter. We did not correct for the reflex motion of the star because its radial-velocity semiamplitude is only known to a 3σ upper limit of $K < 0.649\,\mathrm{km\,s^{-1}}$. This upper limit is below the $\sim$0.8 km s^{-1} that each pixel represents, and the star is rapidly rotating ($v \sin i_\star = 99.85^{+0.64}_{-0.61}$ km s^{-1}), which means that correcting for the stellar motion would not significantly impact the results (Casasayas-Barris et al. 2018). This choice also ensures the deep static Na I features, most likely due to interstellar medium absorption, are removed in later stages of the analysis.

To keep the ratio between the average flux of the different orders constant, we normalized the average flux of each order to the average flux of that order over time. While this process removes information about the average flux in each exposure, this information is taken into account when combining the different in-transit exposures (see Section 4.2.1). We then performed sigma clipping to remove cosmics and other outliers that were not corrected in the data reduction process: after stacking all exposures, we ran a sliding 40 pixel window that replaced flux values farther than 5σaway from the mean by the interpolation of their neighboring pixels. Finally, we masked the spectral regions with evident sky emission and the spectral lines that were not accurately modeled by `molecfit`, notably the deep telluric lines in the oxygen B-band ($\sim$6900 Å see Figure 1).

3.1.1. Atmospheric Model Templates

The atmosphere of a planet filters the light of the star during the planet transit. The different gases that compose the atmosphere absorb the light at different wavelengths, causing the apparent size of the planet to change with wavelength. The transmission spectra models calculate how the planet size changes for various combinations of atmospheric gases and planet bulk parameters. In this work, we search for neutral and singly ionized metals with atomic number up to 28 and with significant spectral features in the wavelength range covered by HARPS-N. This includes Al I, Ca I, Ca II, Co I, Cr I, Cr II, Fe I, Fe II, K I, Mg I, Mn I, Mn II, Na I, Ni I, Sc I, Sc II, Si I, Ti I, Ti II, V I, and V II.

We calculated the absorption cross sections for the different gases using the open-source and custom opacity calculator `HELIOS-K` (Grimm et al. 2021). `HELIOS-K` is a very efficient opacity calculator that runs on graphics processing units (GPUs). As input to calculate the gas opacities, we used the line-list tables from Kurucz (2018), assumed Voigt line profiles for the absorption lines, 0.01 cm^{-1} spectral resolution, and a constant line cutoff of 100 cm^{-1}. To calculate the transmission spectra, we developed our code based on the simple formalism presented in Gaidos et al. (2017) and Bower et al. (2019). Our

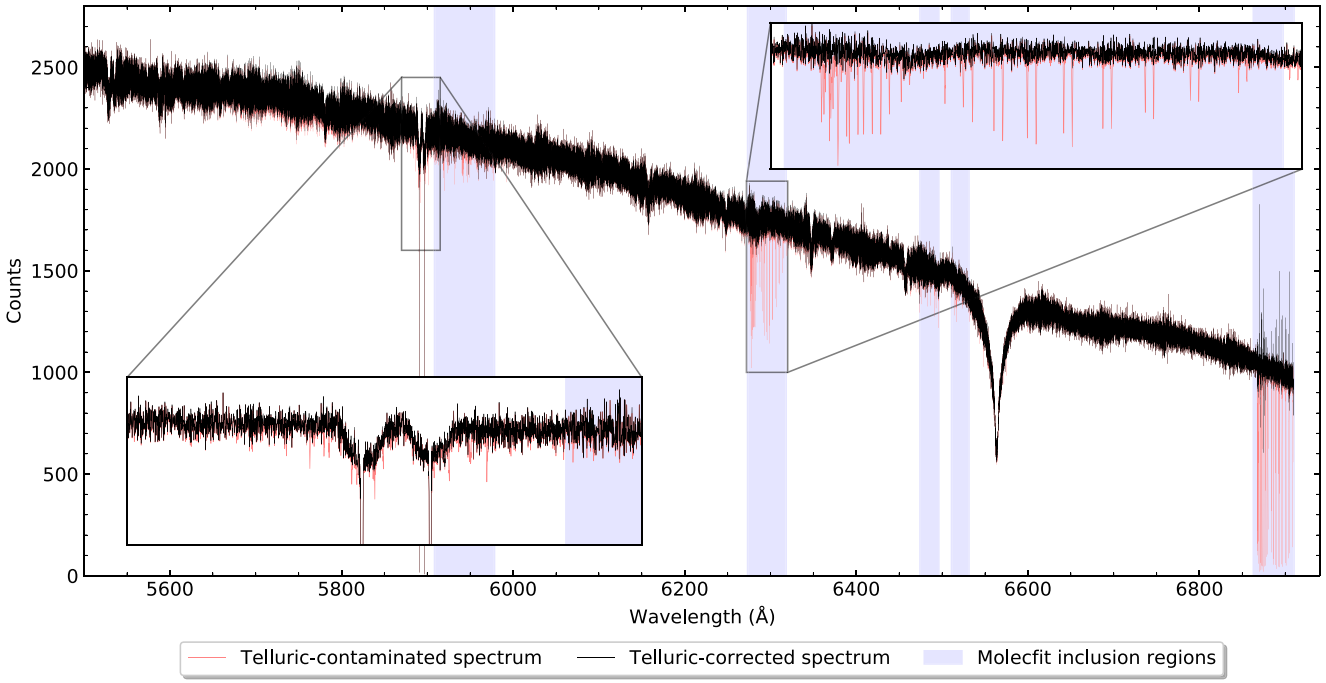

Figure 1. One of the HARPS-N spectra of HAT-P-70 before (red) and after (black) correcting the telluric absorption with `molecfit`. Only the red part of the spectrum is shown, where most telluric lines are found. The regions included in the telluric fit are highlighted in blue. The two insets show in more detail the spectral regions around the Na I doublet (left) and the oxygen γ-band (right). Deep absorption is visible in the core of the stellar Na I doublet, which we attribute to interstellar medium absorption.

model computes the effective tangent height in an atmosphere that was discretized in 200 annuli. The chemical concentration calculations were done using the open-source code FastChem (Stock et al. 2018) assuming solar metallicities, except for the species Sc I and Sc II which are not included in the open-source version of FastChem. For Sc I and Sc II, we considered a constant mixing ratio of 10^{-8}, which is a simple first-order approximation to search for possible detections. We included in our model the H^- bound-free and free–free absorption from John (1988). Each high-resolution transmission spectrum includes one gas species along with H^- continuum absorption and scattering by H and H_2. The surface gravity of the planet was set to $\log g = 3$, and the atmosphere was assumed to be in isothermal conditions, with a temperature of 4000 K. HAT-P-70b orbits an A-type star, and we therefore expect the atmospheric temperature at the pressures probed in transmission spectroscopy to be significantly higher than the planetary equilibrium temperature (Lothringer & Barman 2019; Stangret et al. 2020).

In addition to the atomic exploration, we also search for the presence of molecules using the ExoMol line-list database. We focus on MgH (Yadin et al. 2012), SiH (Yurchenko et al. 2018), and TiO (McKemmish et al. 2019), as these species present multiple spectral features in the visible range and can potentially withstand the high temperatures of HAT-P-70b. We set the temperature of these models to 4000 K, except for MgH, which we set to 3000 K because there were no data available at 4000 K. We present these models, together with the atomic models, in Figure 2.

The templates were then broadened using a Gaussian kernel to match the spectral resolving power of HARPS-N, $R = 115{,}000$. The continuum, obtained by a quadratic spline interpolation of the highest values in each 30 Å window, is then removed from each model template. Those values smaller than 1×10^{-4} times the value of the deepest line in each template were set to zero (Hoeijmakers et al. 2020a). Following subtraction of the continuum, these models served as cross-correlation templates.

3.1.2. Cross Correlations with the Model Templates

The cross-correlation function coefficients $c(v, t)$ were calculated according to:

$$c(v, t) = \sum_{i=0}^{N} x_i(t) T_i(v), \quad (1)$$

where $x_i(t)$ is the flux at the ith pixel in the spectrum obtained at time t, and $T_i(v)$ is the atmospheric template Doppler-shifted by a velocity v, which takes values ranging from -500 to 500 km s^{-1} in steps of 1 km s^{-1}. N indicates the total number of pixels in each spectrum, accross all orders. The spectra were neither continuum normalized nor blaze corrected. Assuming photon noise is the dominant noise source, the weight of each pixel in the sum of Equation (1) is therefore proportional to its variance, without the need for explicit weights (Hoeijmakers et al. 2020a). To obtain the cross-correlation functions (CCFs) corresponding to the transmission signal, all coefficients were subsequently divided by the average of those located out of transit. We applied a Gaussian filter of width 70 km s^{-1} to remove any remaining broadband variations (Hoeijmakers et al. 2020a).

In the resulting CCFs, the radial velocity of the planet $v_p(t)$ is given by

$$v_p(t) = K_p \sin(2\pi\phi(t)) + v_{\rm sys}, \quad (2)$$

where K_p is the planet radial-velocity semiamplitude, $\phi(t)$ is the orbital phase at time t, and $v_{\rm sys}$ is the systemic velocity.

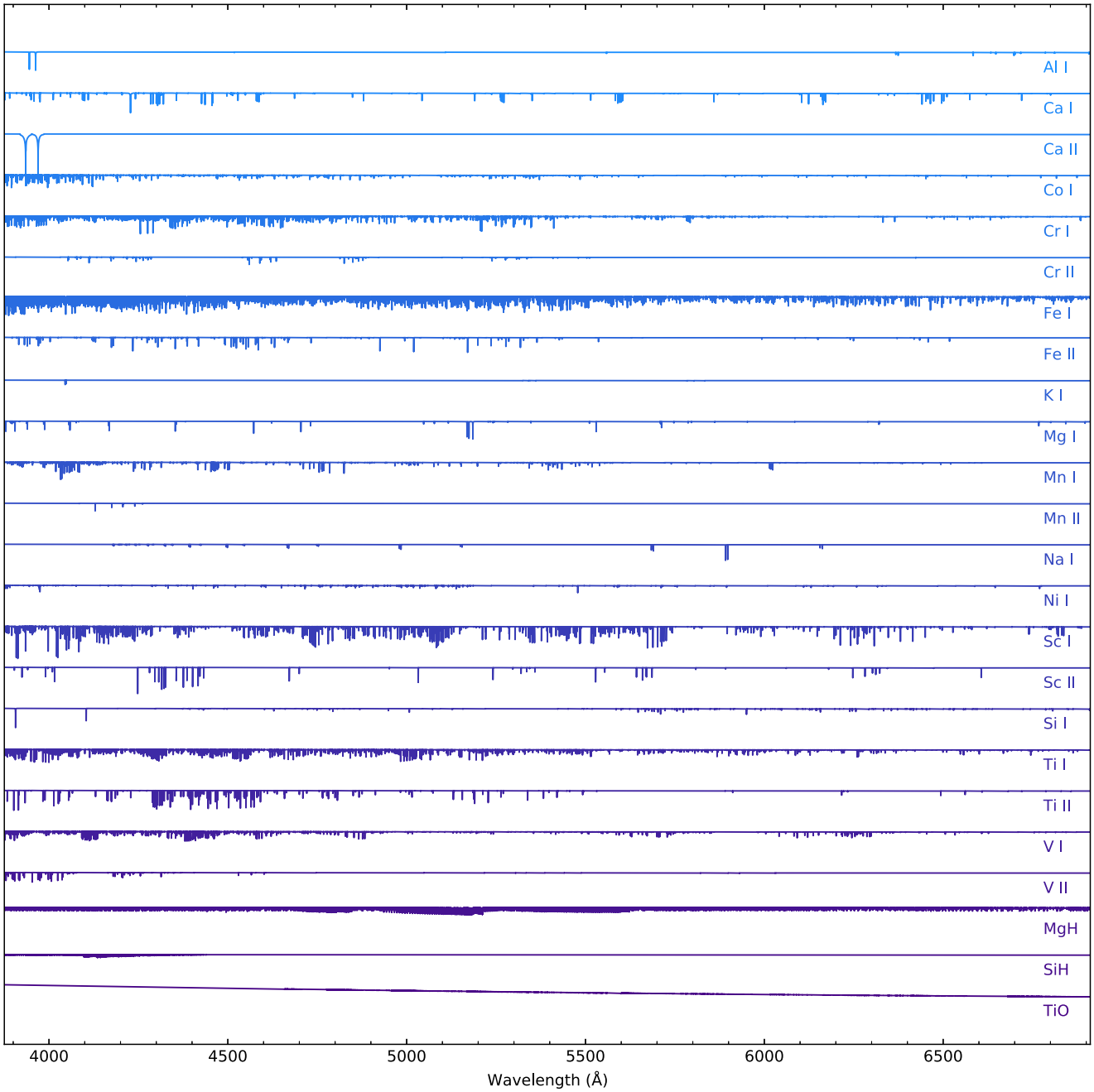

Figure 2. High-resolution models for each of the species surveyed in this work. These models are on the same scale (except for TiO, which is scaled up by a factor of 20), with a constant offset between each of them for clarity.

3.1.3. Spin–Orbit Alignment

During the planetary transit, the rotationally broadened line profiles of the stellar spectrum are distorted by the planet blocking part of the stellar disk. This generates a time-dependent signal in the CCFs of those species present in the star, known as the Doppler shadow (Collier Cameron et al. 2010). The Doppler shadow could potentially bias the results from the cross-correlation analysis, and therefore we removed it from the CCFs—for this purpose, we performed a direct spectral modeling approach, which we describe in Section 3.1.4. Here, we focus on how we used the Doppler shadow as a powerful source of information about the architecture of the system. In particular, we used the location of the Doppler shadow in each CCF to derive the angle between the orbital axis of the planet and the spin axis of the star, also known as spin–orbit angle or obliquity.

For each epoch, the velocity in the cross-correlation function at which the Doppler shadow appears corresponds to the line-of-sight velocity of the part of the stellar disk occulted by the planet. Ignoring differential rotation and convection, this velocity is given by

$$v_{\rm occ}(t) = x_{\perp} v \sin i_{\star}, \tag{3}$$

where $v \sin i_{\star}$ is the apparent rotational velocity of the star, and $x_{\perp}$ is the orthogonal distance from the planet to the stellar spin

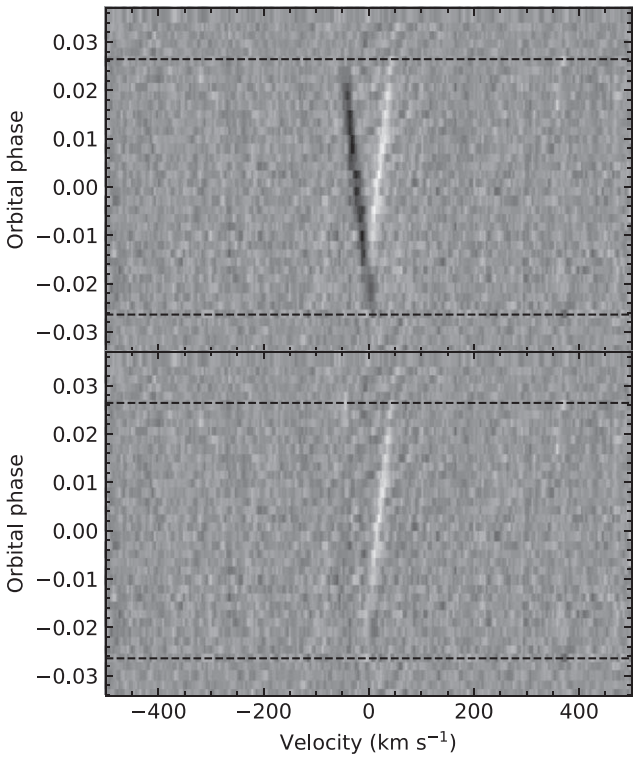

Figure 3. Removal of the Doppler shadow. Top: CCFs that result from cross correlating the different exposures with a PHOENIX template and dividing by the master out-of-transit CCF. The black dashed lines mark the beginning and end of the transit. The black slanted streak, visible during transit, is caused by the planet blocking part of the stellar disk and is known as the Doppler shadow. The white slanted streak is the planet atmosphere signal. Bottom: same as above, but in this case the spectra were corrected for the Rossiter-McLaughlin and center-to-limb variation effects priors to cross correlation, as described in Section 3.1.4, which caused the Doppler shadow to disappear.

axis. This distance can be expressed as

$$x_{\perp} = \frac{a}{R_{\star}}(\sin(2\pi\phi)\cos\lambda + \cos(2\pi\phi)\cos i_p \sin\lambda), \quad (4)$$

where a is the orbital semimajor axis, $R_{\star}$ is the stellar radius, λ is the obliquity and i_p is the orbital inclination (Cegla et al. 2016).

Following Hoeijmakers et al. (2019), we used a high-resolution synthetic spectrum from the PHOENIX library (Husser et al. 2013) with an effective temperature of $T_{\rm eff} = 8400$ K and surface gravity of $\log g = 4.00$, values that closely resemble those of the host star. This PHOENIX template was then treated similarly to the atmospheric model templates: it was continuum normalized and broadened to match the instrumental resolution of HARPS-N, and it was used thereafter to produce the CCFs. Cross correlating the spectra with a PHOENIX template yields two strong signals: the Doppler shadow and the exoplanet atmosphere signal, as shown in Figure 3. We approximated the Doppler shadow in each in-transit CCF with a Gaussian function, ignoring the exposures where its velocity was close to that of the atmosphere signal.

We then conducted a Markov Chain Monte Carlo (MCMC) analysis of the Doppler shadow, similar to that in Hoeijmakers et al. (2020b). We used the centroids $v_{\rm occ}^{\rm obs}(t)$ and centroid uncertainties $\sigma_v^{\rm obs}(t)$ from the Gaussian fit of the Doppler shadow in each in-transit CCF, and assumed a Gaussian log-likelihood function

$$L \propto -\frac{1}{2}\sum_t \left(\frac{v_{\rm occ}^{\rm obs}(t) - v_{\rm occ}^{\rm mod}(t)}{\sigma_v^{\rm obs}(t)} \right)^2, \quad (5)$$

where $v_{\rm occ}^{\rm mod}(t)$ is the line-of-sight velocity of the part of the stellar disk occulted by the planet at time t. Our model parameters include $v \sin i_{\star}$, $a/R_{\star}$, λ, i_p and $v_{\rm sys}$. We used a uniform prior for the obliquity ($0° < \lambda < 360°$) and Gaussian priors for the parameters derived from the transit light-curve analysis in Zhou et al. (2019) ($a/R_{\star}$ and i_p), with the mean and standard deviation shown in Table 1. We also used Gaussian priors for $v \sin i_{\star}$ and for $v_{\rm sys}$, each with a conservative standard deviation of 5 km s^{-1} to account for potential offsets from the spectroscopic measurements in Zhou et al. (2019). We sampled the posterior distributions with the `emcee` Python package (Foreman-Mackey et al. 2013).

Table 1
Results of the MCMC Analysis of the Doppler Shadow

Parameter	Symbol	Unit	Prior	Posterior
Scaled semimajor axis	$a/R_{\star}$	⋯	$\mathcal{N}(5.45, 0.49)$	$5.23^{+0.46}_{-0.47}$
Orbital inclination	i_p	°	$\mathcal{N}(96.5, 1.4)$	$95.47^{+0.80}_{-0.73}$
Obliquity	λ	°	$\mathcal{U}(0, 360)$	$107.9^{+2.0}_{-1.7}$
Projected stellar rotational velocity	$v \sin i_{\star}$	km s^{-1}	$\mathcal{N}(99.9, 5.0)$	$98.6^{+5.0}_{-4.9}$
Systemic velocity	$v_{\rm sys}$	km s^{-1}	$\mathcal{N}(25.2, 5.0)$	$25.0^{+4.6}_{-4.7}$

Note. $\mathcal{N}(\mu, \sigma)$ indicates a Gaussian distribution with mean μ (from Zhou et al. 2019) and standard deviation σ, while $\mathcal{U}(a, b)$ denotes a uniform distribution from a to b. The last column shows the median value derived for each parameter. The 16th and 84th percentiles are used to establish the uncertainties.

3.1.4. Modeling the Rossiter-McLaughlin and Center-to-limb Variation Effects

The spectrum across a stellar disk is not uniform. The spectrum originating in each region of the stellar disk is Doppler-shifted by an amount proportional to the projected rotational velocity and the distance to the stellar spin axis. Additionally, the line profile changes as a function of the limb angle $\mu = \cos\theta$, where θ is the angle between the line of sight and the normal to the stellar surface. Recent works in exoplanet transmission spectroscopy have highlighted the importance of correcting for these two effects, known as the Rossiter-McLaughlin and center-to-limb variation effects, as they can significantly impact the results, potentially leading to false negatives and false positives (e.g., Czesla et al. 2015; Yan et al. 2017; Chen et al. 2020; Casasayas-Barris et al. 2021).

When combining the different transmission spectra in the rest frame of a planet on a near-polar orbit such as HAT-P-70b, the spectral signature produced by the Rossiter-McLaughlin effect largely smears out. The center-to-limb variation effect is also unlikely to substantially alter the results of our analysis, as this effect is generally weaker in hot stars and HAT-P-70 has one of the highest effective temperatures among all known exoplanet hosts. For completeness, we still chose to model these effects, following the steps outlined in Cabot et al. (2020).

Using `Spectroscopy Made Easy` version 522 (SME, Piskunov & Valenti 2017), the Vienna Atomic Line Database

(VALD, Ryabchikova et al. 2015) and the Kurucz ATLAS9 model atmospheres (Castelli & Kurucz 2003), we computed stellar spectra at 21 limb angles, ranging from the center of the stellar disk to the limb in steps of $\Delta\mu = 0.05$. We used the stellar parameters in Zhou et al. (2019). We divided the stellar disk in square cells with side length $0.01\,R_\star$ and assigned to each cell a spectrum that we obtained from linear interpolation of the 21 reference spectra. The spectrum of each cell is Doppler-shifted by the line-of-sight velocity of that cell assuming no differential rotation.

At the orbital phase of each exposure we integrated the spectra in the cells blocked by the planet disk. The radius of this disk was set to that of HAT-P-70b and its coordinates were calculated with Equation (4) and

$$y_\perp = \frac{a}{R_\star}(\sin(2\pi\phi)\sin\lambda - \cos(2\pi\phi)\cos i_p \cos\lambda), \quad (6)$$

using the parameters derived from the Doppler shadow analysis in Section 3.1.3. These integrated spectra were then divided by the stellar spectrum (obtained from the integration of the spectra in all cells of the stellar disk), continuum normalized using a cubic polynomial and broadened to match the resolution of HARPS-N. We then used these spectra to correct the two-dimensional spectra prior to cross correlation, which resulted in the removal of the Doppler shadow from the CCFs (see Figure 3).

3.2. Transmission Spectroscopy

Often, the discoveries of atomic species in ground-based, high-resolution, exoplanet transmission spectra involve a cross-correlation approach to combine the S/N of multiple lines. However, some species can be identified through a single prominent spectral feature, such as the Na I doublet, the Ca II H and K lines, and the H I Balmer lines. To search for these prominent spectral lines, we derived the transmission spectrum of HAT-P-70b. Our analysis was similar to that of Cabot et al. (2020), with slight modifications as described below.

After performing sigma clipping on the two-dimensional spectra, we divided each order by the corresponding blaze function and Doppler-shifted them to the HAT-P-70 rest frame using the systemic velocity and the Earth's barycentric velocity. We did not correct for the reflex motion of the star due to the reasons outlined in Section 3.1. As in the cross-correlation analysis, we corrected for the Rossiter-McLaughlin and center-to-limb variation effects using the spectra computed in Section 3.1.4.

We produced the master stellar spectrum by combining all out-of-transit spectra:

$$\hat{f}_{\rm out}(\lambda) = \sum_{t_{\rm out}} w(\lambda, t_{\rm out}) f(\lambda, t_{\rm out}), \quad (7)$$

where $f(\lambda, t_{\rm out})$ corresponds to the flux at the wavelength λ at an out-of-transit time $t_{\rm out}$. We weighted these fluxes by $w(\lambda, t_{\rm out})$, the inverse of their squared uncertainties (calculated assuming photon noise) to account for the changes in S/N throughout the observations.

Each spectrum was then divided by this master out-of-transit spectrum to produce the transmission spectra:

$$\Re(\lambda, t) = \frac{f(\lambda, t)}{\hat{f}_{\rm out}(\lambda)}. \quad (8)$$

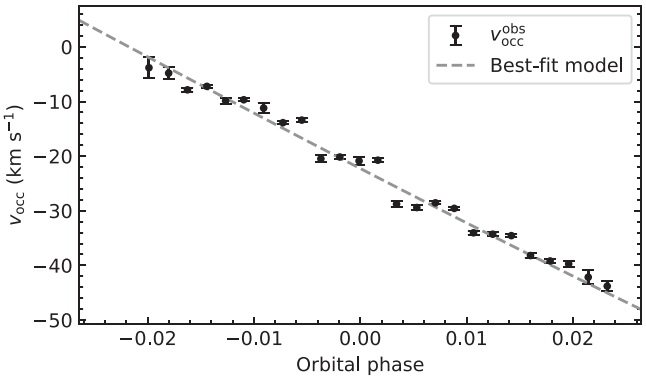

Figure 4. Best-fit model of the Doppler shadow. The black dots correspond to the centroid velocities of the Gaussian fits to each of the CCFs that make up the Doppler shadow of Figure 3. To avoid contamination from the atmosphere of HAT-P-70b, we discard measurements at velocities that are close to the radial velocity of the exoplanet signal. The gray dashed line marks the best-fit model that results from the evaluation of Equation (5).

To normalize the transmission spectra, we fit a linear function to each spectrum and divided it out. Cabot et al. (2020) used a fifth-degree polynomial in the normalization process, but their analysis involved the stitched spectrum that combines all orders from HARPS. Our analysis is on an order-by-order basis, so a linear polynomial suffices. We found significant residuals in the core of the stellar Na I doublet. We masked out these residuals during the analysis so as to not influence the results.

We then Doppler-shifted all transmission spectra to the planet rest frame using the planet radial velocity given by Equation (2). We obtained the master transmission spectrum by a weighted average of the in-transit normalized transmission spectra. We removed any residual broadband variations using a median filter with a width of 1501 pixels (Cabot et al. 2020).

4. Results and Discussion

4.1. A Planet on a Nearly Polar Orbit

Our MCMC analysis of the Doppler shadow, described in Section 3.1.3, consists of 100 walkers of 100,000 steps each. We discard the first 5,000 steps to avoid sampling during the burn-in phase, and thin the chains by 800 (approximately the auto-correlation time). Table 1 lists the values derived from our analysis, and Figure 4 presents the measurements of the centroid velocities and the best-fit model. Figure 10 shows the posterior distributions.

Zhou et al. (2019) find an obliquity of $\lambda = 113.1^{\circ}{}^{+5.1}_{-3.4}{}^{\circ}$ by simultaneously modeling the light curve and the Doppler shadow. According to the classification in Addison et al. (2018), this value corresponds to a retrograde orbit ($112\overset{\circ}{.}5 \leqslant |\lambda| \leqslant 247\overset{\circ}{.}5$). In this work, we update the value of the obliquity of HAT-P-70b to $\lambda = 107.9^{\circ}{}^{+2.0}_{-1.7}{}^{\circ}$, indicative of a nearly polar orbit ($67\overset{\circ}{.}5 < |\lambda| < 112\overset{\circ}{.}5$ and $247\overset{\circ}{.}5 < |\lambda| < 292\overset{\circ}{.}5$). Like many other hot Jupiters found around hot stars, HAT-P-70b shows a highly misaligned orbit (Winn et al. 2010).

4.2. Results from the Cross-correlation Analysis

From our cross-correlation analysis, we claim the detection (i.e., a signal with S/N > 4 at a location consistent with that of the planet) of the following neutral and ionized species in the

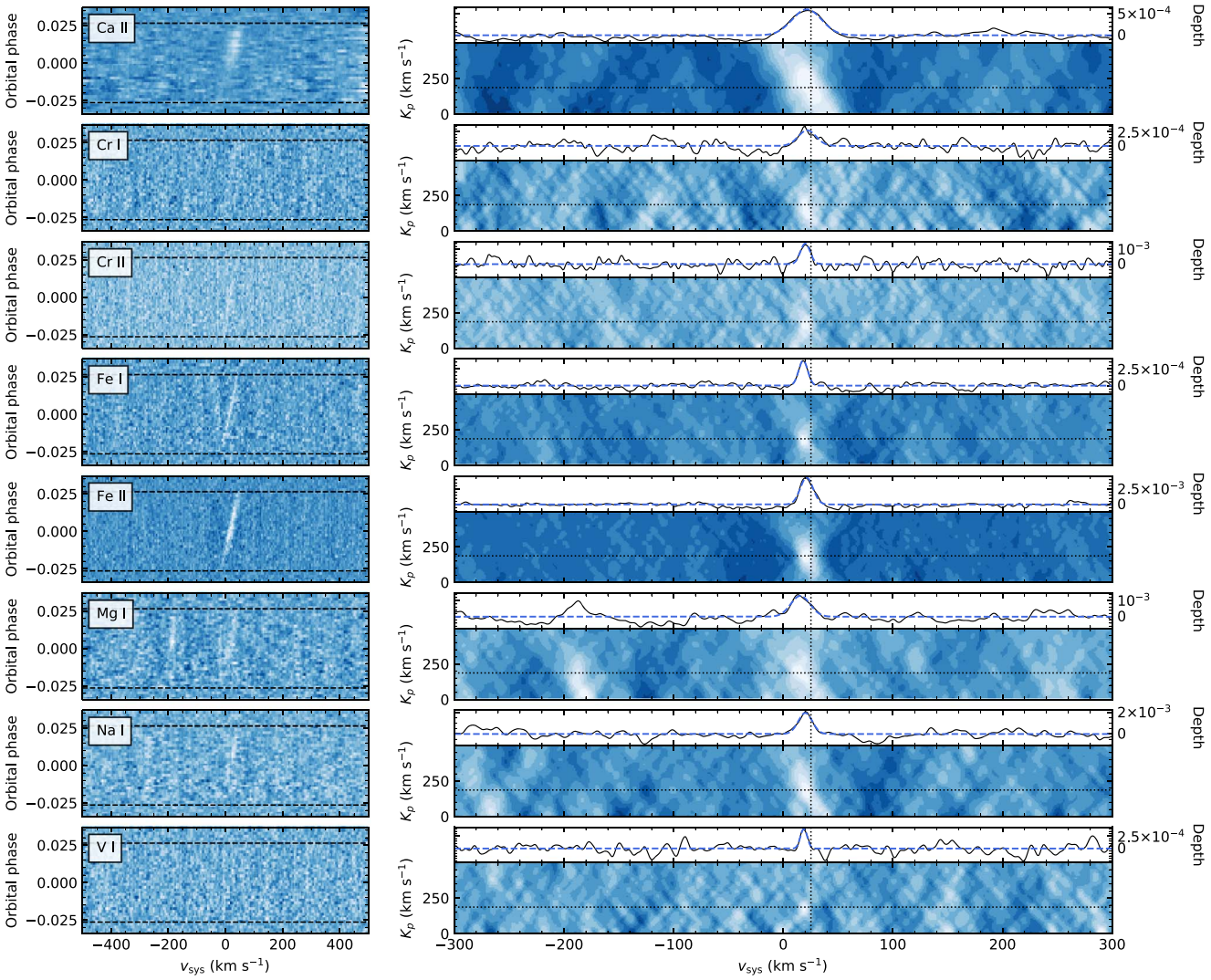

Figure 5. Detection of various neutral and ionized species in the atmosphere of HAT-P-70b. Left: CCFs of the species for which we claim a detection (Ca II, Cr I, Cr II, Fe I, Fe II, Mg I, Na I, and V I). The CCFs are in the rest frame of the solar system barycenter. The Doppler shadow has already been removed. The horizontal dashed lines mark the beginning and end of the transit. The slanted white streak visible during the transit corresponds to the planet atmosphere. Right: $K_p - v_{sys}$ maps, with the in-transit CCFs coadded at different planet radial-velocity semiamplitudes (i.e., along different slopes) and at different systemic velocities. The dotted lines indicate the expected systemic velocity and radial-velocity semiamplitude of the planet (Zhou et al. 2019). The values at the expected planet radial-velocity semiamplitude, $K_p = 187$ km s^{-1}, are plotted above each $K_p - v_{sys}$ map, fitted with a Gaussian model. In the case of Mg I, the peak near $v_{sys} = -190$ km s^{-1} is caused by contamination from one of the strongest Fe II lines.

atmosphere of HAT-P-70b: Ca II, Cr I, Cr II, Fe I, Fe II, Mg I, Na I, and V I. We also present tentative evidence (i.e., with $3 \leqslant S/N \leqslant 4$) of Ca I and Ti II that will require further investigation.

4.2.1. Detection of Ca II, Cr I, Cr II, Fe I, Fe II, Mg I, Na I, and V I

In this section, we present the detection of Ca II, Cr I, Cr II, Fe I, Fe II, Mg I, Na I, and V I in HAT-P-70 b via the cross-correlation method. The panels in the left column of Figure 5 show the CCFs that result from cross correlating the HARPS-N data set with model templates of these species. The slanted white streak, discernible during transit, corresponds to the atmospheric signal.

To combine the signal from the in-transit CCFs, we construct $K_p - v_{sys}$ diagrams by taking the weighted average of the in-transit cross-correlation coefficients along different planet radial-velocity semiamplitudes K_p and systemic velocities v_{sys} (Brogi et al. 2012). The weights correspond to the mean flux in each exposure (Hoeijmakers et al. 2020a). We sample planet radial-velocity semiamplitudes between 0 and 500 km s^{-1} and systemic velocities between −300 and 300 km s^{-1}, in steps of 1 km s^{-1}.

The resulting $K_p - v_{sys}$ diagrams are presented in the right column of Figure 5. We convert the cross-correlation coefficients to S/N values by dividing them by the standard deviation of the coefficients located at systemic velocities farther than 50 km s^{-1} from where we expect the planet signal (e.g., Brogi & Line 2019; Stangret et al. 2020). We measure enhancements in the cross-correlation coefficients near the predicted location of the exoplanet, with S/N values ranging from 4.7 (V I) to 17.6 (Fe II). In Table 2, we present the velocity pair (i.e., K_p and v_{sys}) and the peak S/N values for each of the species for which we claim a detection.

The coadded cross-correlation coefficients at the expected radial-velocity semiamplitude of the exoplanet ($K_p =$ 187 km s^{-1}, calculated according to the orbital parameters in

Table 2
Results from the Cross-correlation Analysis for the Species for Which We Claim a Detection and for the Species for Which We Only Find Tentative Evidence (Marked with an Asterisk)

Species	Strongest Signal		Gaussian Fit at $K_p = 187$ km s^{-1}			
	S/N_{max}	$\{K_p, v_{sys}\}_{max}$	A ($\times 10^{-3}$)	Δv_{sys} (km s^{-1})	FWHM (km s^{-1})	$\Delta R_p/R_p$
Ca I *	3.2	$\{144^{+65}_{-44}, 21^{+5}_{-3}\}$	0.39 ± 0.12	-3.0 ± 1.2	8.2 ± 2.9	0.020 ± 0.006
Ca II	9.0	$\{236^{+74}_{-163}, 18^{+15}_{-5}\}$	0.59 ± 0.03	-3.8 ± 0.8	31.5 ± 1.9	0.030 ± 0.002
Cr I	4.8	$\{172^{+59}_{-90}, 20^{+5}_{-3}\}$	0.28 ± 0.05	-3.4 ± 1.7	19.3 ± 4.0	0.014 ± 0.003
Cr II	6.6	$\{154^{+27}_{-17}, 20^{+1}_{-2}\}$	1.40 ± 0.22	-5.2 ± 0.8	10.4 ± 1.9	0.069 ± 0.011
Fe I	11.1	$\{169^{+21}_{-18}, 19^{+1}_{-2}\}$	0.37 ± 0.03	-7.1 ± 0.4	9.7 ± 1.0	0.019 ± 0.002
Fe II	17.6	$\{177^{+34}_{-24}, 21^{+1}_{-2}\}$	4.37 ± 0.17	-3.9 ± 0.3	13.7 ± 0.6	0.203 ± 0.009
Mg I	5.2	$\{192^{+47}_{-91}, 13^{+11}_{-4}\}$	1.31 ± 0.18	-9.6 ± 1.4	20.7 ± 3.3	0.065 ± 0.009
Na I	6.1	$\{180^{+61}_{-53}, 21^{+2}_{-4}\}$	1.95 ± 0.24	-5.2 ± 0.9	15.1 ± 2.1	0.095 ± 0.011
Ti II *	3.6	$\{102^{+201}_{-45}, 13^{+5}_{-5}\}$	0.49 ± 0.10	-13.2 ± 1.8	17.4 ± 4.2	0.025 ± 0.005
V I	4.7	$\{161^{+44}_{-26}, 19^{+2}_{-2}\}$	0.40 ± 0.09	-6.5 ± 0.8	7.3 ± 2.0	0.020 ± 0.005

Note. For each species we indicate the maximum S/N in the $K_p - v_{sys}$ diagram (S/N_{max}) and the velocity pair ($\{K_p, v_{sys}\}_{max}$) at which this maximum S/N occurs. We also indicate the best-fit Gaussian parameters (amplitude, velocity offset and full width at half maximum) of the CCFs at the expected planet radial-velocity semiamplitude, $K_p = 187$ km s^{-1} (Zhou et al. 2019), and express the amplitude as an excess planet radius in units of planet radii ($\Delta R_p/R_p$).

Zhou et al. 2019) are plotted above each $K_p - v_{sys}$ diagram. We fit these cross-correlation coefficients by a Gaussian function using the Levenberg–Marquardt algorithm to determine the depth, Doppler shift and width of each signal. As in Hoeijmakers et al. (2019), we set the uncertainty in the data as the standard deviation of the values at $|\Delta v_{sys}| > 50$ km s^{-1}, far from the planetary signal. Our Gaussian function fit only includes every fourth data point. This is because the atmospheric model templates were broadened to match the spectral resolution of HARPS-N (see Section 3.1.1), meaning that the correlation length in the resulting CCFs is $\Delta v_{sys} \approx 3$ km s^{-1} (Collier Cameron et al. 2010; Hoeijmakers et al. 2020a). Table 2 summarizes the results of the Gaussian fits.

The amplitudes of the different signals span an order of magnitude, from 0.28×10^{-3} (Cr I) to 4.37×10^{-3} (Fe II). These amplitudes indicate the excess transit depth associated with each species. We can express this excess transit depth, $\Delta\delta$, as an excess planet radius, ΔR_p:

$$\frac{\Delta R_p}{R_p} = \sqrt{\frac{(R_p/R_\star)^2 + \Delta\delta}{(R_p/R_\star)^2}} - 1. \quad (9)$$

Table 2 shows the excess planet radius of each species. These measurements provide an estimate of the radius at which the cores of a weighted average of the spectral lines become optically thick, and therefore depend on the line opacities and the abundance profile of each species.

Various factors contribute to the broadening of the lines in the transmission spectrum of exoplanet atmospheres, including winds, instrumental broadening, Doppler broadening caused by the atomic thermal motion, and pressure broadening due to collisions with other particles. The rotation of the planet can also broaden the line profiles to a level detectable by high-resolution spectroscopy (Snellen et al. 2014). Given the tidal forces expected at such short orbital distances, HAT-P-70b is likely to have a synchronous rotation such that its orbital period and rotational period are the same (Rasio et al. 1996; Brogi et al. 2016). This would induce a rotational broadening of ~ 3.5 km s^{-1}. Additionally, according to Equation (2), the planet changes radial velocity by about ~ 2 km s^{-1} during each exposure, which would further contribute to smearing out the signal. Thanks to the remarkable strength of the Fe I and Fe II signals in HAT-P-70b, we are able to measure their FWHMs with high precision. We find that the signal of Fe II is significantly broader than that of Fe I, potentially caused by the larger velocity range at the low pressures probed by Fe II (Gibson et al. 2020).

The centroid measurements in Table 2 indicate that all signals are blueshifted from the exoplanet rest frame by a few km s^{-1}. This blueshift might be due to the presence of strong winds flowing at low pressures from the day side to the night side of the planet, driven by the large day–night heating gradients in extremely irradiated gas giants like HAT-P-70b (Showman et al. 2013; Komacek & Showman 2016). Additionally, the blueshifts are slightly different for the different species. For example, there is a significant difference in the blueshifts of the Fe I and Fe II signals, with Fe I experiencing a blueshift ~ 3 km s^{-1} larger than that of Fe II. As the signals originate at different altitudes in the atmosphere, these differences can be explained by a stratification of the atmosphere (Hoeijmakers et al. 2020b; Nugroho et al. 2020b). Blueshifts larger in Fe I than in Fe II have also been reported in the transmission spectrum of other ultrahot Jupiters, including MASCARA-2 b (Casasayas-Barris et al. 2019; Hoeijmakers et al. 2020b; Nugroho et al. 2020b; Stangret et al. 2020) and WASP-121 b (Ben-Yami et al. 2020; Bourrier et al. 2020; Gibson et al. 2020; Hoeijmakers et al. 2020a; Borsa et al. 2021). A significantly blueshifted spectral signature of Fe I has also been detected in the ultrahot Jupiter WASP-76 b (Ehrenreich et al. 2020; Tabernero et al. 2021). Per contra, the Fe I and Fe II detections in KELT-9 b show no significant Doppler shift with respect to the rest frame of the planet (Hoeijmakers et al. 2019). Cabot et al. (2021) recently reported a detection of Fe I in the atmosphere of the ultrahot Jupiter TOI-1518b, blueshifted by ~ 2 km s^{-1}, and a tentative detection of Fe II, with a blueshift of ~ 4 km s^{-1}.

We also note that determining the Doppler shifts of the atmospheric spectral signatures with respect to the planet relies on the accurate measurement of the systemic radial velocity of the star. The systemic velocity used in our analysis is from Zhou et al. (2019), derived by modeling the stellar line profiles from a least-squares deconvolution using spectra taken by the

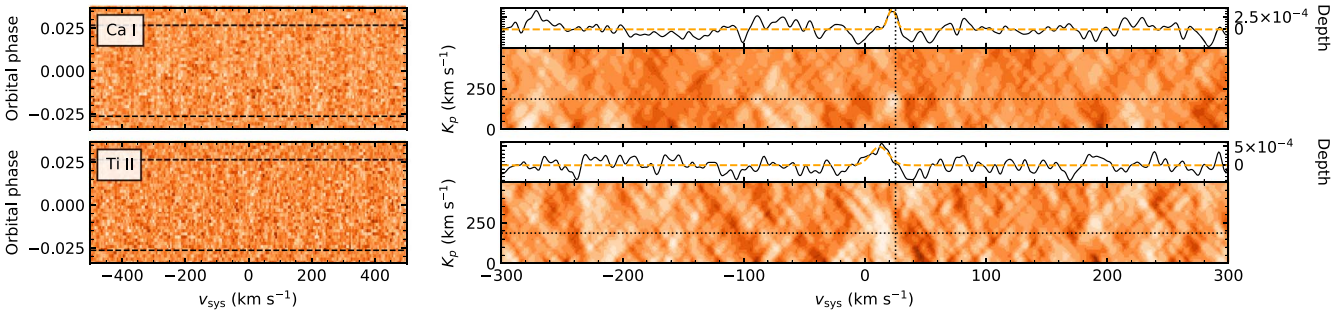

Figure 6. Same as Figure 5, but for the species for which we find tentative evidence rather than claiming a detection.

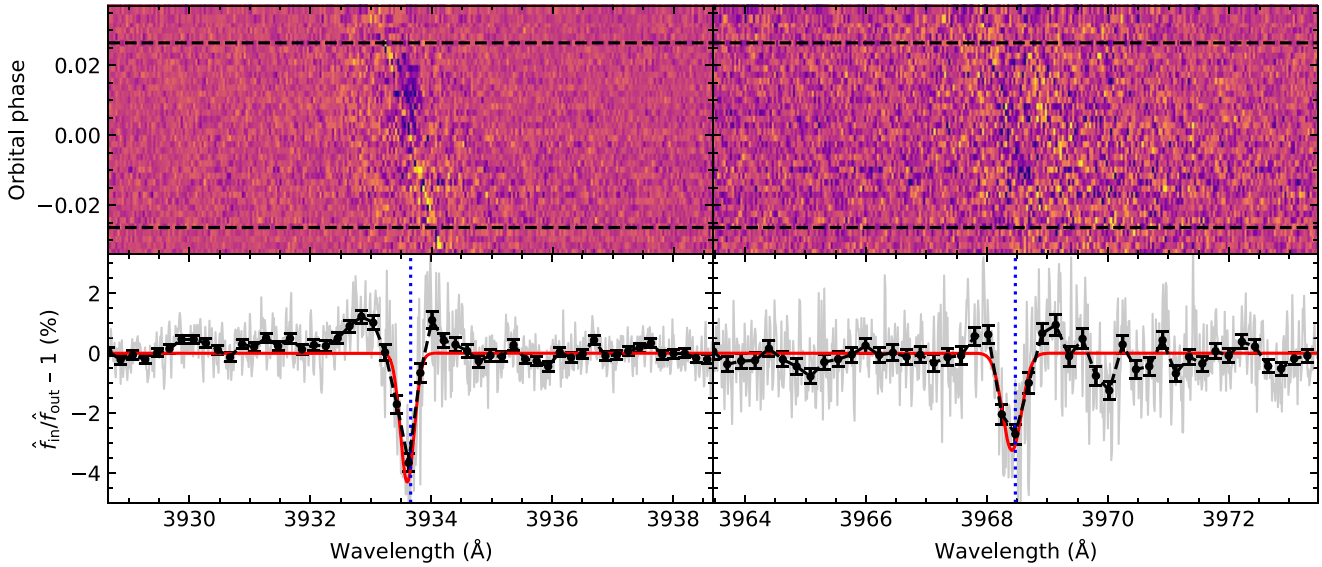

Figure 7. Transmission spectroscopy for the Ca II K (left) and H (right) lines. Top row: Residuals in the exoplanet rest frame, obtained by dividing the spectrum at each orbital phase by the master out-of-transit spectrum and correcting for the contribution from the RM and CLV effects. The horizontal dashed lines mark the beginning and end of the transit. Bottom row: unbinned (gray) and 20x binned (black) master transmission spectrum, fitted with a Gaussian model (red). The vertical blue dotted line indicates the theoretical location of each spectral line.

Tillinghast Reflector Echelle Spectrograph (TRES). As pointed out by Hoeijmakers et al. (2019), different radial-velocity derivation methods for rapidly rotating stars could result in differences in the systemic velocity of a few km s^{-1}. Our Doppler shadow analysis provides an alternative, less precise value for the systemic velocity of the system. This value is still larger than the systemic velocities at which we detect the different species, giving us confidence that the blueshifts are likely not due to the determination of the systemic velocity.

4.2.2. Tentative Evidence of Ca I and Ti II

Besides the detections presented above, we also find tentative evidence of Ca I and Ti II (Figure 6). The velocity pair of the Ca I signal is consistent with that of the planet and of the other detected species. However, its S/N peaks at 3.2, which is below our detection threshold of 4. Also below the detection threshold is the signal of Ti II, which peaks at $S/N_{max} = 3.6$. The Ti II signal has a K_p value consistent with that of the planet, and it is markedly extended and blueshifted in the $K_p - v_{sys}$ map. The CCFs of Ti II present significant noise near $v_{sys} = 0$ km s^{-1}, which affects the $K_p - v_{sys}$ map.

Table 3
Results from the Transmission Spectroscopy Analysis

Line	Depth (%)	Δv_{sys}	FWHM
Ca II H	3.25 ± 0.37	-4.2 ± 1.6	28.3 ± 3.7
Ca II K	4.30 ± 0.36	-4.2 ± 0.9	20.7 ± 2.0
Hα	1.56 ± 0.15	-2.5 ± 1.6	34.1 ± 3.9
Hβ	0.80 ± 0.14	6.8 ± 2.8	32.9 ± 6.7
Hγ	1.07 ± 0.18	-6.8 ± 3.1	36.5 ± 7.2
Na I D1	0.61 ± 0.15	-2.7 ± 1.2	10.1 ± 2.9
Na I D2	0.70 ± 0.14	-6.1 ± 1.1	12.3 ± 2.6

Note. For each spectral feature, we indicate the depth, velocity offset (in km s^{-1}) and FWHM (in km s^{-1}), derived from the Gaussian fit.

4.3. Results from the Transmission Spectroscopy Analysis

4.3.1. Detection of Ca II H and K Lines

As shown in Figure 7, the individual Ca II H and K lines are clearly detected despite their location near the blue end of the spectrum (3968.47 Å and 3933.66 Å, respectively).

As in the cross-correlation analysis, the Ca II lines appear blueshifted by a few km s^{-1} with respect to their predicted location (Table 3).

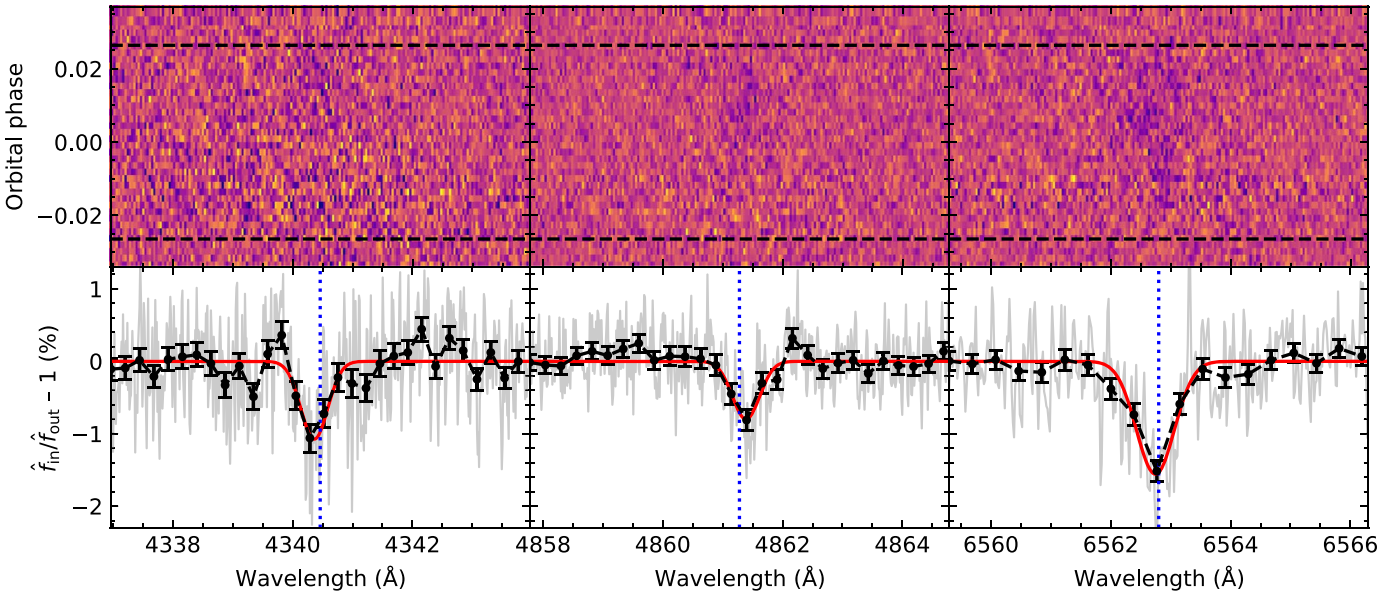

Figure 8. Same as Figure 7, but for Hγ (left), Hβ (middle), and Hα (right).

The Ca II H and K lines have larger absolute depths than those reported in WASP-33 b and KELT-9 b (Yan et al. 2019). We can use Equation (9) to calculate the excess planet radii for each of the Ca II lines in HAT-P-70 b: $\Delta R_p/R_p = 1.08 \pm 0.09$ for the H line, and $\Delta R_p/R_p = 1.32 \pm 0.08$ for the K line. These values imply the presence of this ionized species at very high altitudes. Ca II appears to be common in the extended atmospheres of ultrahot Jupiters (Casasayas-Barris et al. 2019; Yan et al. 2019; Nugroho et al. 2020b; Tabernero et al. 2021; Turner et al. 2020; Borsa et al. 2021; Merritt et al. 2021), where it outnumbers Ca I. The H and K lines are the dominant spectral features in the Ca II high-resolution models (Figure 2).

Using the planet mass upper limit of $M_p < 6.78\,M_J$ set by Zhou et al. (2019), the Roche lobe radius of HAT-P-70 b is $R_{Roche}/R_p < 4$ (Eggleton 1983). If $(R_p + \Delta R_p) > R_{Roche}$ (i.e., if $M_p \lesssim 1.3\,M_J$), then that would indicate that Ca II is escaping from the atmosphere.

4.3.2. Detection of Hα, Hβ, and Hγ

In addition to the species found by cross correlation, the transmission spectroscopy analysis reveals one more species: H I. In particular, we detect absorption by the Hα (6562.80 Å), Hβ (4861.28 Å) and Hγ (4340.46 Å) Balmer lines (Figure 8). Their corresponding excess transit depths ($\Delta R_p/R_p$) are 0.61 ± 0.05, 0.35 ± 0.05 and 0.45 ± 0.07, respectively. This suggests that HAT-P-70 b has an extended atmosphere where hydrogen atoms become excited by the extreme ultraviolet (EUV) radiation coming from the host star, as previously observed in other ultrahot Jupiters around A-type stars, such as KELT-9 b (Yan & Henning 2018; Cauley et al. 2019; Wyttenbach et al. 2020), MASCARA-2 b (Casasayas-Barris et al. 2018, 2019) and WASP-33 b (Cauley et al. 2021; Yan et al. 2021). Excess Hα absorption has also been reported in ultrahot Jupiters orbiting cooler stars, such as WASP-12 b (Jensen et al. 2018) and WASP-121 b (Cabot et al. 2020; Borsa et al. 2021), and it can be indicative of an outflowing envelope (Yan & Henning 2018). The simultaneous detection of Hα, Hβ, and Hγ in HAT-P-70b offers the opportunity to constrain the temperature structure of its upper atmosphere (Fossati et al. 2020; Wyttenbach et al. 2020) and investigate a potential Balmer-driven hydrodynamic escape (García Muñoz & Schneider 2019).

4.3.3. Detection of the Na I Doublet

In Figure 9 we show the transmission spectrum in the region of the Na I doublet. We find absorption at the location of the Na I D1 (5895.924 Å) and D2 (5889.951 Å) lines, with similar excess transit depths ($\Delta R_p/R_p = 0.27 \pm 0.06$ and $\Delta R_p/R_p = 0.31 \pm 0.06$). Both features are blueshifted by a few km s^{-1} from their expected location, consistent with the results in the cross-correlation analysis.

5. Conclusions

In this work we present the first analysis of the transmission spectrum of the ultrahot Jupiter HAT-P-70b using high-resolution data from HARPS-N. Using a cross-correlation analysis, we detect eight neutral and singly ionized atomic species (Ca II, Cr I, Cr II, Fe I, Fe II, Mg I, Na I, and V I) and find tentative evidence of Ca I and Ti II. These species appear blueshifted by a few km s^{-1}, consistent with winds that have a predominantly subsolar–antisolar circulation pattern, similar to other ultrahot Jupiters (e.g., Nugroho et al. 2020b; Stangret et al. 2020; Borsa et al. 2021). Additionally, via transmission spectroscopy, we individually resolve the Ca II H and K lines (formed at very low pressures), the Na I doublet and the Hα, Hβ, and Hγ lines, which indicate the presence of an extended H I envelope.

HAT-P-70b joins the family of ultrahot Jupiters with a chemically rich spectrum. We emphasize that, despite the high number of species we detected in HAT-P-70b and the remarkable strength of some of them (e.g., Fe II), the work presented here only used a single-transit event with HARPS-N —further studies could reveal additional species and allow for a detailed investigation of the atmospheric dynamics of HAT-P-70b (Seidel et al. 2021; Wardenier et al. 2021). HAT-P-70b is also a promising target for emission spectroscopy to investigate the chemistry of its day side (e.g., Nugroho et al. 2020a;

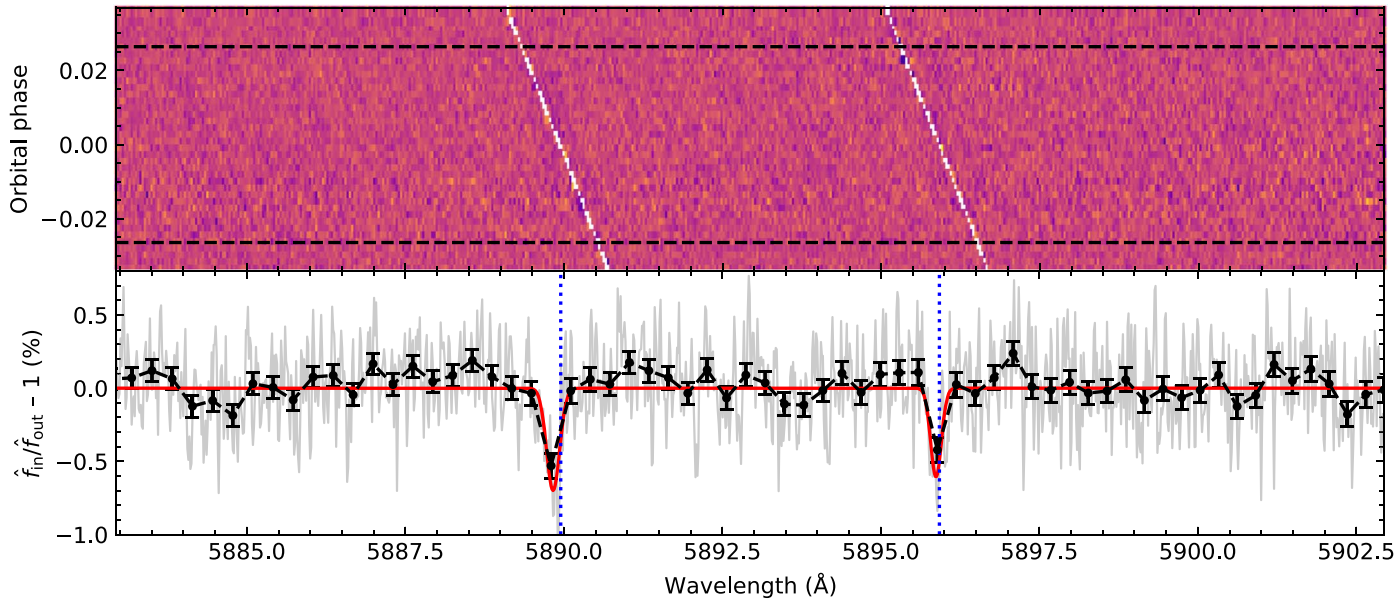

Figure 9. Same as Figure 7, but for the Na I doublet. The atmospheric signal appears as a dark, vertical trail (top panel). The white trails are the masked out artifacts from the interstellar medium absorption lines.

Pino et al. 2020) and a possible temperature inversion (Lothringer & Barman 2019; Malik et al. 2019).

We thank the anonymous referee for a thoughtful report, which improved the quality of the manuscript. We also thank René Tronsgaard for enlightening discussions preparing the HARPS-N observations, Avet Harutyunyan for performing the observations, and Simon Albrecht for helpful insight on the obliquity analysis. A.B.-A. gratefully acknowledges support from "la Caixa" Foundation (ID 100010434), under agreement LCF/BQ/EU19/11710067. This work is based on observations made with the Italian Telescopio Nazionale Galileo (TNG) operated on the island of La Palma by the Fundación Galileo Galilei of the INAF (Istituto Nazionale di Astrofisica) at the Spanish Observatorio del Roque de los Muchachos of the Instituto de Astrofisica de Canarias. This work has made use of the VALD database, operated at Uppsala University, the Institute of Astronomy RAS in Moscow, and the University of Vienna.

Facility: TNG (HARPS-North).

Software: astropy (Astropy Collaboration et al. 2013), `corner` (Foreman-Mackey 2016), `emcee` (Foreman-Mackey et al. 2013), `HELIOS-K` (Grimm et al. 2021), `matplotlib` (Hunter 2007), `molecfit` (Kausch et al. 2015; Smette et al. 2015), `numpy` (Harris et al. 2020), `PyAstronomy` (Czesla et al. 2019), `scipy` (Virtanen et al. 2020), `spectres` (Carnall 2017).

Appendix
Doppler Shadow Posteriors

Figure 10 presents the posteriors from the MCMC analysis of the Doppler shadow, used to measure the obliquity of HAT-P-70b. We also plot the impact parameter ($b = a\cos i_p/R_\star$). Although b is not an independent parameter, including it in Figure 10 helps to visualize the correlation between different parameters.

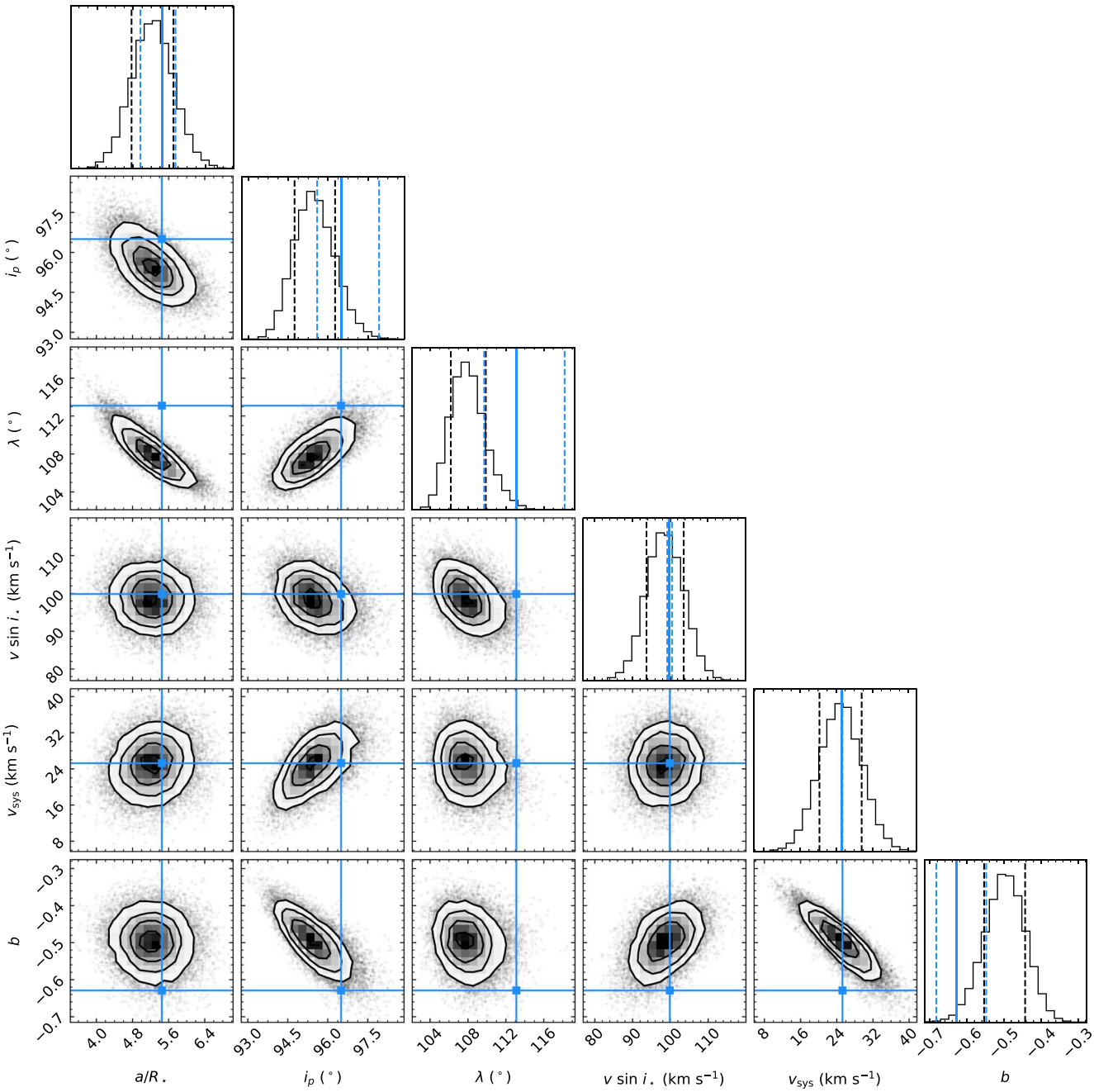

Figure 10. Corner plot of the posteriors of our MCMC analysis of the Doppler shadow. The black dashed lines in the histograms correspond to the 16th and 84th percentiles. The blue solid lines indicate the values in Zhou et al. (2019), with the corresponding uncertainty intervals marked by blue dashed lines.

ORCID iDs

Aaron Bello-Arufe https://orcid.org/0000-0003-3355-1223
Samuel H. C. Cabot https://orcid.org/0000-0001-9749-6150
João M. Mendonça https://orcid.org/0000-0002-6907-4476
Lars A. Buchhave https://orcid.org/0000-0003-1605-5666
Alexander D. Rathcke https://orcid.org/0000-0002-4227-4953

References

Addison, B. C., Wang, S., Johnson, M. C., et al. 2018, AJ, 156, 197
Arcangeli, J., Désert, J.-M., Line, M. R., et al. 2018, ApJL, 855, L30
Astropy Collaboration, Robitaille, T. P., Tollerud, E. J., et al. 2013, A&A, 558, A33
Bell, T. J., & Cowan, N. B. 2018, ApJL, 857, L20
Ben-Yami, M., Madhusudhan, N., Cabot, S. H. C., et al. 2020, ApJL, 897, L5
Birkby, J. L. 2018, arXiv:1806.04617
Borsa, F., Allart, R., Casasayas-Barris, N., et al. 2021, A&A, 645, A24
Bourrier, V., Ehrenreich, D., Lendl, M., et al. 2020, A&A, 635, A205
Bower, D. J., Kitzmann, D., Wolf, A. S., et al. 2019, A&A, 631, A103
Brogi, M., de Kok, R. J., Albrecht, S., et al. 2016, ApJ, 817, 106
Brogi, M., & Line, M. R. 2019, AJ, 157, 114
Brogi, M., Snellen, I. A. G., de Kok, R. J., et al. 2012, Natur, 486, 502
Cabot, S. H. C., Bello-Arufe, A., Mendonça, J. M., et al. 2021, AJ, 162, 218
Cabot, S. H. C., Madhusudhan, N., Welbanks, L., Piette, A., & Gandhi, S. 2020, MNRAS, 494, 363
Carnall, A. C. 2017, arXiv:1705.05165
Casasayas-Barris, N., Palle, E., Stangret, M., et al. 2021, A&A, 647, A26
Casasayas-Barris, N., Pallé, E., Yan, F., et al. 2018, A&A, 616, A151
Casasayas-Barris, N., Pallé, E., Yan, F., et al. 2019, A&A, 628, A9
Castelli, F., & Kurucz, R. L. 2003, in IAU Symp. 210, Modelling of Stellar Atmospheres, Poster Contributions, ed. N. Piskunov, W. W. Weiss, & D. F. Gray (San Francisco, CA: ASP), A20

Cauley, P. W., Shkolnik, E. L., Ilyin, I., et al. 2019, AJ, 157, 69
Cauley, P. W., Wang, J., Shkolnik, E. L., et al. 2021, AJ, 161, 152
Cegla, H. M., Lovis, C., Bourrier, V., et al. 2016, A&A, 588, A127
Chen, G., Casasayas-Barris, N., Pallé, E., et al. 2020, A&A, 635, A171
Clough, S. A., Shephard, M. W., Mlawer, E. J., et al. 2005, JQSRT, 91, 233
Collier Cameron, A., Bruce, V. A., Miller, G. R. M., Triaud, A. H. M. J., & Queloz, D. 2010, MNRAS, 403, 151
Cosentino, R., Lovis, C., Pepe, F., et al. 2012, Proc. SPIE, 8446, 84461V
Czesla, S., Klocová, T., Khalafinejad, S., Wolter, U., & Schmitt, J. H. M. M. 2015, A&A, 582, A51
Czesla, S., Schröter, S., Schneider, C. P., et al. 2019, PyA: Python astronomy-related packages, Astrophysics Source Code Library, ascl:1906.010
Eggleton, P. P. 1983, ApJ, 268, 368
Ehrenreich, D., Lovis, C., Allart, R., et al. 2020, Natur, 580, 597
Foreman-Mackey, D. 2016, JOSS, 1, 24
Foreman-Mackey, D., Hogg, D. W., Lang, D., & Goodman, J. 2013, PASP, 125, 306
Fossati, L., Shulyak, D., Sreejith, A. G., et al. 2020, A&A, 643, A131
Gaidos, E., Kitzmann, D., & Heng, K. 2017, MNRAS, 468, 3418
Gao, P., Thorngren, D. P., Lee, G. K. H., et al. 2020, NatAs, 4, 951
García Muñoz, A., & Schneider, P. C. 2019, ApJL, 884, L43
Gibson, N. P., Merritt, S., Nugroho, S. K., et al. 2020, MNRAS, 493, 2215
Grimm, S. L., Malik, M., Kitzmann, D., et al. 2021, ApJS, 253, 30
Harris, C. R., Millman, K. J., van der Walt, S. J., et al. 2020, Natur, 585, 357
Helling, C., Lewis, D., Samra, D., et al. 2021, A&A, 649, A44
Heng, K. 2016, ApJL, 826, L16
Hoeijmakers, H. J., Cabot, S. H. C., Zhao, L., et al. 2020b, A&A, 641, A120
Hoeijmakers, H. J., Ehrenreich, D., Heng, K., et al. 2018, Natur, 560, 453
Hoeijmakers, H. J., Ehrenreich, D., Kitzmann, D., et al. 2019, A&A, 627, A165
Hoeijmakers, H. J., Seidel, J. V., Pino, L., et al. 2020a, A&A, 641, A123
Hunter, J. D. 2007, CSE, 9, 90
Husser, T. O., Wende-von Berg, S., Dreizler, S., et al. 2013, A&A, 553, A6
Jensen, A. G., Cauley, P. W., Redfield, S., Cochran, W. D., & Endl, M. 2018, AJ, 156, 154
John, T. L. 1988, A&A, 193, 189
Kausch, W., Noll, S., Smette, A., et al. 2015, A&A, 576, A78
Kesseli, A. Y., & Snellen, I. A. G. 2021, ApJL, 908, L17
Kitzmann, D., Heng, K., Rimmer, P. B., et al. 2018, ApJ, 863, 183
Komacek, T. D., & Showman, A. P. 2016, ApJ, 821, 16
Kurucz, R. L. 2018, in ASP Conf. Ser. 515, Workshop on Astrophysical Opacities, ed. C. Mendoza et al. (San Francisco, CA: ASP), 47
Langeveld, A. B., Madhusudhan, N., Cabot, S. H. C., & Hodgkin, S. T. 2021, MNRAS, 502, 4392
Lothringer, J. D., & Barman, T. 2019, ApJ, 876, 69
Lothringer, J. D., Barman, T., & Koskinen, T. 2018, ApJ, 866, 27
Lothringer, J. D., Rustamkulov, Z., Sing, D. K., et al. 2021, ApJ, 914, 12
Malik, M., Kitzmann, D., Mendonça, J. M., et al. 2019, AJ, 157, 170
McKemmish, L. K., Masseron, T., Hoeijmakers, H. J., et al. 2019, MNRAS, 488, 2836
Merritt, S. R., Gibson, N. P., Nugroho, S. K., et al. 2021, MNRAS, 506, 3853
Nugroho, S. K., Gibson, N. P., de Mooij, E. J. W., et al. 2020a, ApJL, 898, L31
Nugroho, S. K., Gibson, N. P., de Mooij, E. J. W., et al. 2020b, MNRAS, 496, 504
Parmentier, V., Line, M. R., Bean, J. L., et al. 2018, A&A, 617, A110
Pino, L., Désert, J.-M., Brogi, M., et al. 2020, ApJL, 894, L27
Piskunov, N., & Valenti, J. A. 2017, A&A, 597, A16
Rasio, F. A., Tout, C. A., Lubow, S. H., & Livio, M. 1996, ApJ, 470, 1187
Ryabchikova, T., Piskunov, N., Kurucz, R. L., et al. 2015, PhyS, 90, 054005
Seidel, J. V., Ehrenreich, D., Allart, A., et al. 2021, A&A, 653, A73
Showman, A. P., Fortney, J. J., Lewis, N. K., & Shabram, M. 2013, ApJ, 762, 24
Smette, A., Sana, H., Noll, S., et al. 2015, A&A, 576, A77
Snellen, I. A. G., Brandl, B. R., de Kok, R. J., et al. 2014, Natur, 509, 63
Snellen, I. A. G., de Kok, R. J., de Mooij, E. J. W., & Albrecht, S. 2010, Natur, 465, 1049
Stangret, M., Casasayas-Barris, N., Pallé, E., et al. 2020, A&A, 638, A26
Stangret, M., Pallé, E., Casasayas-Barris, N., et al. 2021, A&A, 654, A73
Stock, J. W., Kitzmann, D., Patzer, A. B. C., & Sedlmayr, E. 2018, MNRAS, 479, 865
Tabernero, H. M., Zapatero Osorio, M. R., Allart, R., et al. 2021, A&A, 646, A158
Turner, J. D., de Mooij, E. J. W., Jayawardhana, R., et al. 2020, ApJL, 888, L13
Virtanen, P., Gommers, R., Oliphant, T. E., et al. 2020, NatMe, 17, 261
Wardenier, J. P., Parmentier, V., Lee, E. K. H., Line, M. R., & Gharib-Nezhad, E. 2021, MNRAS, 506, 1258
Winn, J. N., Fabrycky, D., Albrecht, S., & Johnson, J. A. 2010, ApJL, 718, L145
Wyttenbach, A., Mollière, P., Ehrenreich, D., et al. 2020, A&A, 638, A87
Yadin, B., Veness, T., Conti, P., et al. 2012, MNRAS, 425, 34
Yan, F., Casasayas-Barris, N., Molaverdikhani, K., et al. 2019, A&A, 632, A69
Yan, F., & Henning, T. 2018, NatAs, 2, 714
Yan, F., Pallé, E., Fosbury, R. A. E., Petr-Gotzens, M. G., & Henning, T. 2017, A&A, 603, A73
Yan, F., Wyttenbach, A., Casasayas-Barris, N., et al. 2021, A&A, 645, A22
Yurchenko, S. N., Sinden, F., Lodi, L., et al. 2018, MNRAS, 473, 5324
Zhou, G., Huang, C. X., Bakos, G. Á, et al. 2019, AJ, 158, 141